Downloaded from https://www.cambridge.org/core. Sistema Bibliotecario - Universita degli Studi di Genova, on 30 May 2020 at 05:05:56, subject to the Cambridge Core terms of use, available at https://www.cambridge.org/core/terms.
https://doi.org/10.1017/jfm.2020.288

J. Fluid Mech. (2020), *vol.* 894, A25. © The Author(s), 2020.
Published by Cambridge University Press
doi:10.1017/jfm.2020.288

The assembly of freely moving rigid fibres measures the flow velocity gradient tensor

Mattia Cavaiola[1,2], Stefano Olivieri[1,2] and Andrea Mazzino[1,2,†]

[1]Department of Civil, Chemical and Environmental Engineering (DICCA), University of Genova, Via Montallegro 1, 16145, Genova, Italy

[2]INFN, Genova Section, Via Montallegro 1, 16145, Genova, Italy

(Received 13 November 2019; revised 27 January 2020; accepted 7 April 2020)

The motion of an assembly of rigid fibres is investigated for different classes of closed streamline flows, steady or time dependent, two-dimensional or three-dimensional. In our study, the dynamics of the fibre assembly is fully coupled to the flow field by means of a state of the art immersed boundary method. We show that, for sufficiently small Stokes times of the assembly, the whole flow gradient tensor can be accurately reconstructed by simply tracking the fibre assembly and measuring suitable fibre velocity differences evaluated at the fibre ends. Our results strongly suggest the possibility of using rigid fibres (or assemblies of them) to perform multi-point flow measures, either in laboratory or in field: future experiments are therefore mandatory to inquire the feasibility of a new 'fibre tracking velocimetry' technique.

Key words: particle/fluid flow, flow–structure interactions

1. Introduction

Understanding the dynamical behaviour of fibre-like objects dispersed in fluid flow is a relevant issue concerning many environmental and industrial processes, such as pollutant dispersion, microfluidic processing and paper production (du Roure *et al.* 2019). Compared with point-like particles, the dynamics of fibres or, more generally, non-spherical particles, turns out to be more complex due to the additional degrees of freedom related to orientation, so that active research is devoted to improve the comprehension of such fluid–structure interactions.

In the case of rigid particles with ellipsoidal shape and which are sufficiently small to evolve in a Stokes flow with negligible fluid inertia, an analytical expression for the fluid torque acting on the particle was originally derived by Jeffery (1922). Such a result has been later generalized to other shapes and widely exploited in a variety of problems. These include studies on the rheology of suspensions in low-Reynolds-number flow conditions (Butler & Snook 2018), as well as on the dynamics of dispersed fibres in turbulent flows (Voth & Soldati 2017). Focusing on the latter framework, several investigations concerned with both homogeneous

† Email address for correspondence: andrea.mazzino@unige.it

isotropic turbulence (Parsa *et al.* 2012; Ni *et al.* 2015; Sabban, Cohen & van Hout 2017) as well as wall-bounded turbulent flows (Marchioli, Fantoni & Soldati 2010; Marchioli, Zhao & Andersson 2016) reveal useful insights on the preferential alignment experienced by fibres and the correlation statistics between their orientation and vorticity. Additionally, Gustavsson *et al.* (2019) recently focused on the settling of small prolate particles, while the orientation of rod-like particles in Taylor–Couette turbulence was analysed by Bakhuis *et al.* (2019).

Despite its significance, the approach based on Jeffery's solution is justified only if the aforementioned assumptions are satisfied. For example, these no longer apply if the fibre length is larger than the Kolmogorov flow scale (i.e. the Reynolds number at the fibre length scale is not sufficiently small). In fact, the dynamical behaviour of fibres with length well within the inertial range of scales is far less understood and has been considered by only few recent experimental investigations (Bounoua, Bouchet & Verhille 2018; Kuperman, Sabban & van Hout 2019), along with the numerical study of Do-Quang *et al.* (2014) who simulated rigid fibres of finite size in a turbulent channel flow. Furthermore, for Jeffery's solution to hold strictly, it is also required that particle inertia (typically quantified by means of the Stokes number) can be neglected as well (Sabban *et al.* 2017).

A further breakdown for the application of Jeffery's model is for the case of flexible fibres. The dynamics of flexible fibres in low-Reynolds-number flows has been recently reviewed by du Roure *et al.* (2019). For sufficiently small fibres, the typical modelling approach relies here on slender body theory (Cox 1970; Tornberg & Shelley 2004). Using this approach, in particular, the motion of flexible fibres in cellular flows has been extensively studied by Young & Shelley (2007), Wandersman *et al.* (2010) and Quennouz *et al.* (2015), revealing the existence of flow-induced buckling instabilities that are responsible for their complex dynamics, including the possibility of a diffusive behaviour for neutrally buoyant fibres due to such deformation. Moreover, Allende, Henry & Bec (2018) recently investigated the stretching rate and buckling probability of non-inertial flexible fibres in ideal turbulence.

For flexible fibres with finite size, some recent contributions have considered this kind of object as the key ingredient for a novel way of flow measurement. In particular, the possibility of using flexible fibres to quantify two-point statistics has been highlighted by Rosti *et al.* (2018*a*, 2020) in the case of homogeneous isotropic turbulence by means of fully resolved direct numerical simulation. This latter case is very far from the realm of application of Jeffery's model for at least three main reasons. The fibres are elastic, inertial and they do not evolve locally in a linear flow (i.e. their size is well within the inertial range of scales). In this situation, the existence of different fibre flapping states was identified, in some of which the fibre behaves as a proxy of turbulent eddies with size comparable to the fibre length. Two-point statistical quantities, such as the velocity structure functions, were thus acquired simply by tracking the fibre end points in time. Related to this framework, significant contributions regarded the flapping instabilities of flexible filaments interacting with two-dimensional low-Reynolds-number flow (Shelley & Zhang 2011), and similar mechanisms were explored for the purpose of passive locomotion and flow control purposes (Bagheri, Mazzino & Bottaro 2012; Lācis *et al.* 2014, 2017). Along a similar line of reasoning, Hejazi, Krellenstein & Voth (2019) investigated experimentally how to measure fluid velocity gradients using particles made by connections of slender deformable arms, both in the case of two-dimensional (2-D) shear flow and three-dimensional (3-D) turbulence.

Downloaded from https://www.cambridge.org/core. Sistema Bibliotecario - Universita degli Studi di Genova, on 30 May 2020 at 05:05:56, subject to the Cambridge Core terms of use, available at https://www.cambridge.org/core/terms. https://doi.org/10.1017/jfm.2020.288

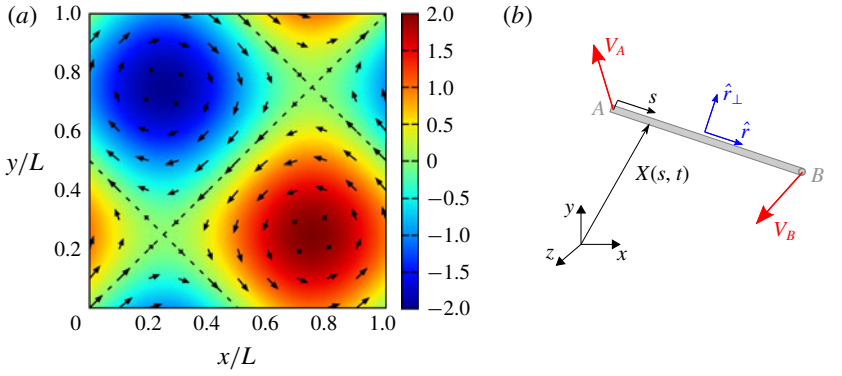

FIGURE 1. (*a*) The so-called BC cellular flow (the colourmap showing the stream function given by (3.1) along with the corresponding velocity vectors); (*b*) sketch of a generic fibre configuration (the characteristic quantities here indicated are introduced in the text).

Motivated by the evidence reported by Rosti *et al.* (2018*a*, 2020), the goal of this work is to investigate similar possibilities for the case of rigid fibres in laminar flow. Rigid fibres are indeed easier to fabricate than elastic ones and are good candidates for novel experimental, non-invasive techniques able to access small-scale, multi-point properties of fluid flows. The idea is to replace single particles, typically used in particle image or tracking velocimetry (PIV/PTV) to measure single-point fluid properties (Adrian 1991; Hoyer *et al.* 2005; Schanz, Gesemann & Schröder 2016), by single fibres (or assemblies of them) in order to access two-point (or multi-point) properties.

To this aim, we will focus on cellular flows, which are also a conceptual representation of eddies of turbulent flows. We will therefore consider spatially periodic solutions of the incompressible Navier–Stokes equations, i.e. the so-called Arnold–Beltrami–Childress (ABC) and Beltrami–Childress (BC) flows (Dombre *et al.* 1986; Biferale *et al.* 1995). A visualization of the latter is given in figure 1(*a*). The choice of this setting will enable us to perform a direct and reliable comparison between the measured fibre velocity and the underlying, unperturbed fluid flow velocity. Although the fibre velocity is generally different from the unperturbed fluid velocity, we will show that the velocities at fibre ends can be used to measure the velocity differences of the unperturbed fluid flow. With unperturbed velocity here we mean the velocity field of the flow in the absence of the fibre. In this framework, a new way for measuring the fluid velocity gradient tensor will be proposed and tested exploiting the assembly of different fibres (three fibres for the two-dimensional incompressible case and eight fibres for the corresponding three-dimensional case). Accessing the velocity gradient is of particular importance when dealing with turbulent flows, since from this quantity one can thus construct the vorticity and strain rate tensors, as well as obtaining the energy dissipation rate and other small-scale quantities.

It is worth summarizing in which sense our model for the fibre dynamics is different with respect to the well known Jeffery's model. In our model the fibre is fully coupled to the flow and it will be of finite size, i.e. its length will be up to the typical size of the cellular flows we will consider. In general, the fibre will thus not be evolving in a linear flow as it is in the Jeffery's model. Moreover, our fibre will be inertial. Different

Downloaded from https://www.cambridge.org/core. Sistema Bibliotecario - Universita degli Studi di Genova, on 30 May 2020 at 05:05:56, subject to the Cambridge Core terms of use, available at https://www.cambridge.org/core/terms.
https://doi.org/10.1017/jfm.2020.288

Stokes numbers will be analysed with the final aim of understanding up to which Stokes numbers a rigid fibre can be used as a proxy of unperturbed flow properties.

Following this introduction, the rest of the paper is structured as follows. In § 2 we present the numerical methods used in the work (complemented by appendix A), § 3 gives the results, and finally § 4 draws some conclusions and perspectives.

2. Methods

We consider an inertial, elastic fibre of length c and diameter $d \ll c$, characterized by (non-dimensional) linear density ρ_1 and bending stiffness γ. Given the position of a material point belonging to the fibre $\boldsymbol{X} = \boldsymbol{X}(s, t)$, as a function of the curvilinear coordinate s and time t, the fibre dynamics is governed by the Euler–Bernoulli's beam equation

$$\rho_1 \ddot{\boldsymbol{X}} = \partial_s(T\partial_s(\boldsymbol{X})) - \gamma \partial_s^4(\boldsymbol{X}) - \boldsymbol{F}. \tag{2.1}$$

In (2.1), $\boldsymbol{F}$ is the forcing exerted by the fluid–structure coupling, while T is the tension necessary to enforce the inextensibility condition

$$\partial_s(\boldsymbol{X}) \cdot \partial_s(\boldsymbol{X}) = 1. \tag{2.2}$$

The fibre is freely moving in the flow, hence the corresponding boundary conditions at its ends are

$$\partial_{ss}\boldsymbol{X}|_{s=0,c} = \partial_{sss}\boldsymbol{X}|_{s=0,c} = 0, \tag{2.3}$$

$$T|_{s=0,c} = 0. \tag{2.4}$$

Nevertheless, we focus here on rigid fibres, as sketched in figure 1(*b*). To this end, throughout the work we choose and retain $c/L = (2\pi)^{-1}$ and $\gamma = 10$ for which we have an essentially rigid behaviour with negligible deformations. The latter can be quantified by looking at the magnitude of the end to end distance, which is always smaller than $O(10^{-8})$.

The fibre is discretized along s into segments with spatial resolution $\Delta s = c/(N_L - 1)$, with N_L being the number of Lagrangian points. To model the fluid–structure coupling, we will consider two different strategies: (i) a fully resolved approach where the feedback is taken into account (which will therefore be denoted as active) and (ii) an intrinsically passive model based on slender body theory. Both strategies are introduced later in this section.

2.1. *Active model*

In the first case the coupling is two-way and the dynamics is resolved using an immersed boundary (IB) technique, inspired by the method proposed by Huang, Shin & Sung (2007) for anchored filaments in laminar flow. The method was also exploited for dispersed fibres in turbulent flow (Rosti *et al.* 2018*a*, 2020; Banaei, Rosti & Brandt 2020). In the present case, we solve numerically the incompressible Navier–Stokes equations for the fluid flow (details on the solution method can be found in appendix A),

$$\partial_t \boldsymbol{u} + \boldsymbol{u} \cdot \boldsymbol{\partial} \boldsymbol{u} = -\boldsymbol{\partial} p/\rho_0 + \nu \partial^2 \boldsymbol{u} + \boldsymbol{f}, \tag{2.5}$$

$$\boldsymbol{\partial} \cdot \boldsymbol{u} = 0, \tag{2.6}$$

Downloaded from https://www.cambridge.org/core. Sistema Bibliotecario - Universita degli Studi di Genova, on 30 May 2020 at 05:05:56, subject to the Cambridge Core terms of use, available at https://www.cambridge.org/core/terms. https://doi.org/10.1017/jfm.2020.288

where $\boldsymbol{u}$ is the fluid velocity, p the pressure, ρ_0 the density and ν the kinematic viscosity. The volumetric forcing $\boldsymbol{f}$ is made by the sum of two contributions: the first is used for generating the desired flow field (Dombre *et al.* 1986), while the second is characteristic of the IB method, mimicking the presence of the fibre by means of no-slip enforcement at the Lagrangian points. Note that the single-mode non-random nature of the volume forcing considered here to generate the flow field does not require the special attention as for the cases considered, for example, by Chouippe & Uhlmann (2015).

When using this approach, we consider a cubic domain of side $L = 2\pi$ with periodic boundary conditions in all directions, which is discretized into a uniformly spaced Cartesian grid using $N = 64$ cells per side. The number of Lagrangian points describing the fibre is chosen in such a way that the Lagrangian spacing Δs is almost equal to that of the Eulerian grid Δx; for example, for a fibre with length $c = 1$ we use $N_L = 11$ Lagrangian points. Doubling both resolutions, the variation of results was found to be negligible. As for the time step we use $\Delta t = 5 \times 10^{-5}$, after assessing the convergence for this parameter as well.

2.2. *Passive model*

In the second approach, a one-way coupling is assumed, i.e. the fibre is forced by the flow but not vice versa. The problem thus essentially consists in solving only (2.1), within which the forcing term is expressed as

$$\boldsymbol{F} = \frac{\rho_1}{\tau_s}\,(\dot{\boldsymbol{X}} - \boldsymbol{u}(\boldsymbol{X}(s,t),t)), \tag{2.7}$$

τ_s being the relaxation time of a fibre immersed in viscous flow, i.e. it can be identified with a Stokes time. Overall, it represents a measure of the fibre inertia compared to the flow, and also quantifies the strength of the coupling. In this approach, $\boldsymbol{u}$ is assigned and does not get modified by the presence of the fibre. Note that our model is similar (apart from the contribution of inertia that we have accounted for in our model) to that of Young & Shelley (2007) and Quennouz *et al.* (2015), relying on local slender body theory, and further simplified assuming an isotropic form for $\boldsymbol{F}$.

Using this model, we assess the convergence of the solution only with the Lagrangian resolution (since there is not the need for an Eulerian grid in this case) and the computational time step. Testing was performed for several initial positions of the fibre and in different cellular flow configurations (i.e. 2-D or 3-D, steady or oscillating). Given the substantially lower computational demand of this approach compared with the active model, for a fibre with length $c = 1$ we choose $N_L = 31$ and $\Delta t = 10^{-6}$, although a numerically stable and resolution-independent solution is already found with coarser resolution, accordingly with our findings for the active case.

3. Results

3.1. *Two-dimensional BC flow*

To start our analysis, we consider the steady and two-dimensional cellular flow, often named as the Beltrami–Childress flow, that is defined by the stream function

$$\Psi(x,y) = \sin(y) - \sin(x), \tag{3.1}$$

Downloaded from https://www.cambridge.org/core. Sistema Bibliotecario - Universita degli Studi di Genova, on 30 May 2020 at 05:05:56, subject to the Cambridge Core terms of use, available at https://www.cambridge.org/core/terms.
https://doi.org/10.1017/jfm.2020.288

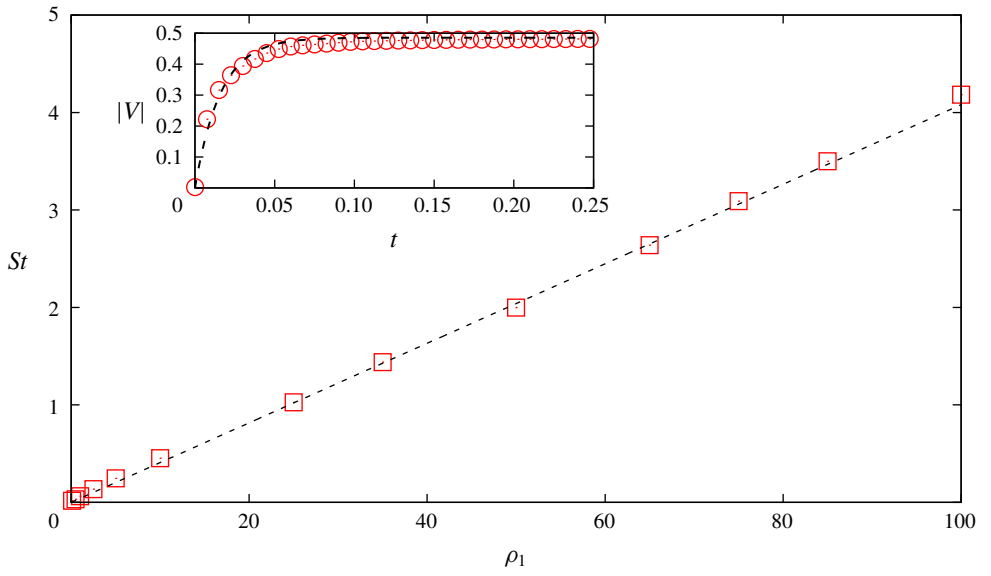

FIGURE 2. Rotational Stokes number as a function of fibre linear density. Red squares, measured values using the active model; black dashed line, linear fit. Inset: time history of the velocity magnitude of one fibre end (red circles) fitted using (3.3) (black dashed line), for a fibre with $\rho_1 = 0.1$.

which is shown in figure 1(*a*). From (3.1), it follows that the velocity field can be expressed as

$$\left.\begin{aligned} u &= \cos y, \\ v &= \cos x. \end{aligned}\right\} \tag{3.2}$$

Such a relatively simple flow configuration will first be used for assessing the importance of fibre inertia by evaluating the rotational Stokes number, and then to present the actual method for measuring two-point velocity differences.

3.1.1. *Rotational Stokes number*

As a preliminary step, we characterize the effect of fibre inertia by estimating the rotational Stokes number, which is the most suitable quantity to consider when dealing with cellular flows such as those considered in this work. This has been done for the sole active fibres, the Stokes number being an assigned parameter in the passive case as shown by (2.7).

To this end, we proceed as follows. We place the fibre at the centre of one cell in the BC flow (figure 1*a*). The fibre is initially at rest and, under the action of the flow, will start to purely rotate around its centre of mass. We measure the time it takes for the fibre to adapt to the flow, i.e. focusing on the velocity magnitude of one fibre end $V(t)$, to assume constant velocity V_0 compatible with the unperturbed fluid velocity. Hence, we perform an exponential fit

$$V(t) = V_0(1 - \mathrm{e}^{-t/\tau_s}) \tag{3.3}$$

to measure the Stokes time τ_s. An example of this procedure is given by the inset of figure 2. From the best fit we obtain the Stokes time and thus the Stokes number defined as $St = \tau_s/\tau_f$, where $\tau_f = c/U$ is the characteristic hydrodynamic time scale

Downloaded from https://www.cambridge.org/core. Sistema Bibliotecario - Universita degli Studi di Genova, on 30 May 2020 at 05:05:56, subject to the Cambridge Core terms of use, available at https://www.cambridge.org/core/terms.
https://doi.org/10.1017/jfm.2020.288

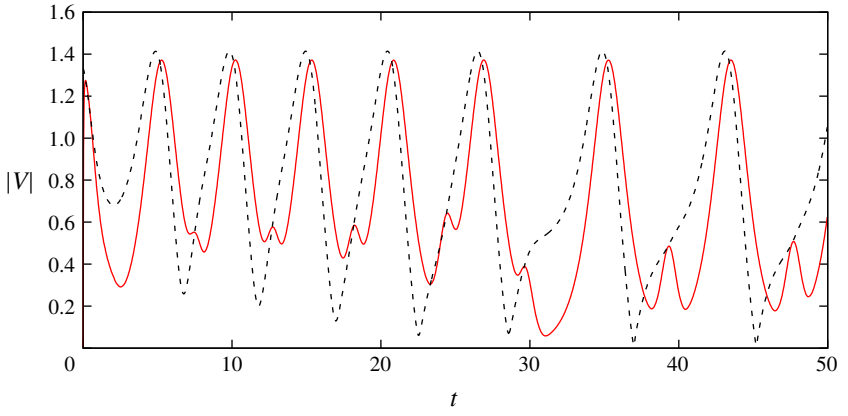

FIGURE 3. Velocity time series at one fibre end for the fibre (red solid line) and for the underlying unperturbed flow (black dashed line), for a fibre with $St \approx 0.01$ released into the BC flow, computed with the active model.

(we choose $U = 1$ as the flow velocity magnitude). The resulting behaviour of St as a function of ρ_1 is depicted in figure 2, showing that it can be well described by a linear law, as expected. Specifically, the best fit of St versus ρ_1 gives $St = \alpha\rho_1$ with $\alpha \approx 0.04$.

Because in the beam equation only one relaxation time is involved in the passive case, its value has been identified as the rotational Stokes time measured in the active case.

3.1.2. *Normal derivative of longitudinal velocity component*

We are now ready to investigate the capability of a rigid fibre to act as a proxy of a laminar, cellular flow in terms of a few fibre properties such as its position and the velocity of the fibre end points. Figure 3 reports the velocity magnitude of one fibre end in time, compared with the velocity magnitude of the unperturbed flow (i.e. in the absence of the fibre) evaluated at the same point. It is evident that the two quantities differ appreciably. This result indicates that a fibre cannot be used to measure single-point flow quantities as done, for example in PIV techniques using tracer particles (Adrian 1991).

Hence, we consider the velocity difference between the fibre end points (figure 1*b*), i.e. $\delta\boldsymbol{V} = \boldsymbol{V}_B - \boldsymbol{V}_A$, and denote by $\delta\boldsymbol{u} = \boldsymbol{u}|_B - \boldsymbol{u}|_A$ the corresponding unperturbed flow velocity difference. Comparing directly these two quantities, however, would still yield the same mismatch previously found for the velocity of one end. Such a mismatch is due not only to the fibre inertia, but also to the fibre inextensibility constraint. Indeed, if we consider the projection of the velocity difference introduced above along the direction parallel to the end to end distance, $\hat{\boldsymbol{r}}$, for a rigid and inextensible object, such a quantity is always zero, although the same quantity for the underlying unperturbed flow is clearly not. Our idea is then to project $\delta\boldsymbol{V}$ on a plane normal to $\hat{\boldsymbol{r}}$ by simply arguing that along that direction the effect of the inextensibility constraint should be washed out. In terms of the normal unit vector $\hat{\boldsymbol{r}}_\perp$ (shown in figure 1*b*), we define the projections,

$$\delta V_\perp = \delta\boldsymbol{V} \cdot \hat{\boldsymbol{r}}_\perp, \tag{3.4}$$

$$\delta u_\perp = \delta\boldsymbol{u} \cdot \hat{\boldsymbol{r}}_\perp. \tag{3.5}$$

Downloaded from https://www.cambridge.org/core. Sistema Bibliotecario - Universita degli Studi di Genova, on 30 May 2020 at 05:05:56, subject to the Cambridge Core terms of use, available at https://www.cambridge.org/core/terms.
https://doi.org/10.1017/jfm.2020.288

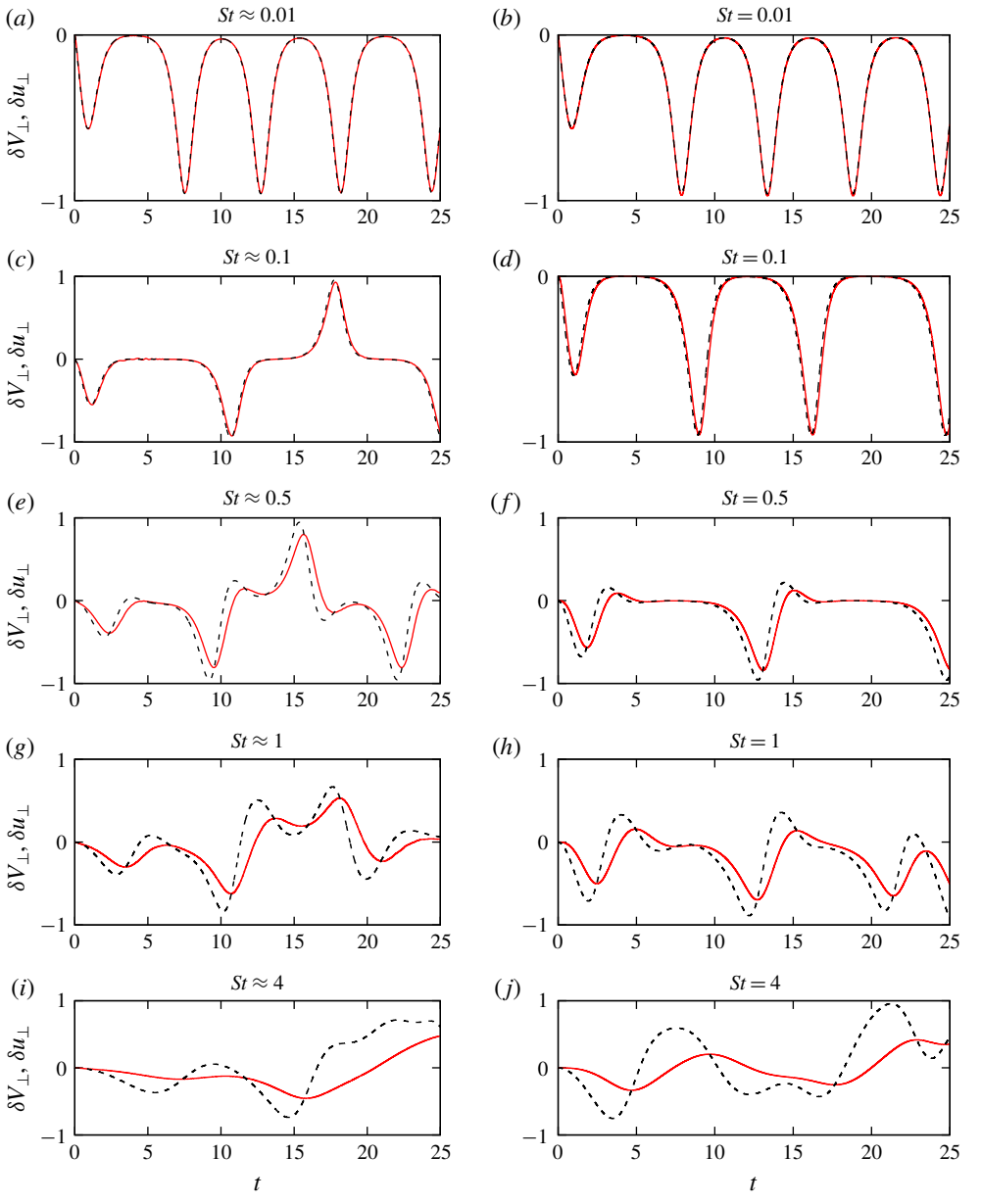

FIGURE 4. Transverse velocity differences of fibre $\delta V_\perp$ (solid line) and unperturbed BC flow $\delta u_\perp$ (dashed line) for different Stokes number, both for the active (*a,c,e,g,i*) and passive (*b,d,f,h,j*) model. The normalized root mean square deviation between $\delta V_\perp$ and $\delta u_\perp$, for both active and passive model, is less than 1 % for $St \leqslant 0.1$, of the order of 10 % for $St \approx 0.5$ and larger than 15 % for $St \geqslant 1$. The fibre length is unity and it is thus approximately 32 % of the size of the single cell in the considered flow.

The projected quantities (3.4) and (3.5) are compared in figure 4 where we report the results of our analysis in the BC flow configuration while varying *St*, for both active and passive models. For relatively low *St* (i.e. the first two rows of the figure), we now notice a remarkable agreement, i.e. the fibre is able to accurately measure the

Downloaded from https://www.cambridge.org/core. Sistema Bibliotecario - Universita degli Studi di Genova, on 30 May 2020 at 05:05:56, subject to the Cambridge Core terms of use, available at https://www.cambridge.org/core/terms.
https://doi.org/10.1017/jfm.2020.288

(unperturbed) flow transverse velocity increments in terms of its transverse velocity increments. For increasing St, i.e. the fibre inertia, the agreement gets worse, as expected. Overall, we observe a close resemblance between results for fibres starting from the same position, using the active (*a,c,e,g,i*) and passive (*b,d,f,h,j*) model, especially for the smallest St. This suggests that here the effective coupling between the flow and the fibre could be actually neglected, in relation to the measurement of transverse velocity differences. Accordingly, when extending our analysis to three-dimensional and unsteady flows (§ 3.2) we will exclusively employ the passive solver on the strength of such evidence.

Nevertheless, figure 4 tells us that the role of feedback cannot be entirely neglected. For sufficiently large Stokes numbers ($St \geqslant 0.1$), the curves on the left panels, (*c,e,g,i*), and those on the right ones, (*d,f,h,j*), are different, revealing that the motion of the fibre centre of mass is affected by the feedback of the fibre to the flow. The effect of the latter is indeed crucial when the fibre centre of mass moves close to the flow separatrix, potentially causing totally different trajectories compared to the passive case.

Some further comments are worth considering. First, the projection along the normal direction to the fibre is crucial for the fibre to be a proxy of the flow velocity differences: if we project the velocity differences along a generic direction, the agreement shown before is no longer present (not shown here). In the two-dimensional case, the normal direction is uniquely defined by $\hat{\boldsymbol{r}}_\perp = \pm(\hat{r}_2, -\hat{r}_1, 0)$. In the three-dimensional case we have instead an infinite number of directions belonging to the normal plane to the fibre orientation. We retain $\hat{\boldsymbol{r}}_\perp = (\hat{r}_2, -\hat{r}_1, 0)$ also for 3-D cases (see § 3.2) even if the results do not change for a different choice of $\hat{\boldsymbol{r}}_\perp$.

The situation considered in figure 4 refers to a fibre whose length is approximately 32 % the size of the single cell. This is a case where the fibre length is sufficiently small compared to the variation scale of the flow. Under such condition the velocity difference between the free ends can be compared with the flow gradient evaluated at the fibre centre of mass. For the latter, the same projection along $\hat{\boldsymbol{r}}_\perp$ has to be applied as before. However, due to the tensorial structure of the gradient $\partial_j u_i$, this translates to considering a double projection, first along the tangential and then along the normal direction,

$$D = \partial_j u_i \hat{r}_j \hat{r}_i^{\perp}. \tag{3.6}$$

In figure 4, where $c/L = (2\pi)^{-1}$, the curve representing D is not reported but would be essentially superimposed onto that of the fluid velocity difference. Doubling the fibre length, i.e. $c/L = \pi^{-1}$, the accuracy gets worse. This simply means that, despite the fact that the fibre accurately measures the transverse velocity differences across the fibre ends, the fibre is too long to allow the derivative to be well approximated by the ratio of the increments.

Finally, another aspect to be considered is the tendency of inertial particles to sample preferential zones of the flow, giving rise to peculiar features such as small-scale clustering of dilute suspensions. This phenomenon is well known and has been thoroughly investigated for spherical particles in turbulent flows (see, e.g. Eaton & Fessler (1994), Bec *et al.* (2006) and Bec *et al.* (2007)) and has also been observed for anisotropic particles (see Voth & Soldati (2017) and references therein). While this mechanism could impact on the potential of using fibres as a proxy of the flow (i.e. measuring only certain regions of space), we highlight that decreasing the Stokes number, along with improving the measure in itself, assures us that at the same time preferential sampling is reduced.

Downloaded from https://www.cambridge.org/core. Sistema Bibliotecario - Universita degli Studi di Genova, on 30 May 2020 at 05:05:56, subject to the Cambridge Core terms of use, available at https://www.cambridge.org/core/terms. https://doi.org/10.1017/jfm.2020.288

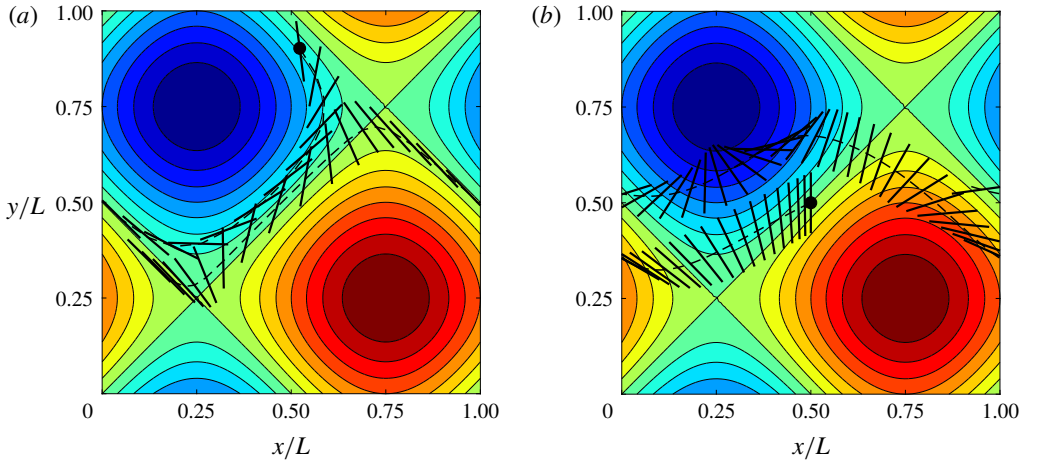

FIGURE 5. Superposition of fibre positions at different instants within the periodic two-dimensional BC flow (the colourmap denoting the stream function), computed with the active model. (*a*) $St = 0.1$ and (*b*) $St = 2$. The dashed line represents the trajectory of fibre centre of mass and the black circle indicates its starting position.

In steady cellular flows, we can easily observe the role of inertia in this regard by looking at the fibre trajectories and, in particular, their deviation from the flow streamlines. A visualization from our data is given in figure 5 where we compare two cases at different St: the less inertial fibre with $St = 0.1$ initially follows the cell streamlines but, due to the centrifugal effect, eventually reaches the flow separation lines (figure 5*a*), while the heavier fibre with $St = 2$ shows a stronger deviation of its trajectory from the streamlines, resulting in a more diffusive behaviour (figure 5*b*).

3.2. *Extension to three-dimensional and unsteady flows*

As a further step, we test the capability of the fibre to measure the transverse velocity differences in three-dimensional steady or unsteady cellular flows. In light of our findings for the steady BC flow (§ 3.1), we present only results obtained with the passive model, although checks using the active model have been performed and yield the same overall scenario as in the steady, two-dimensional case.

First, we consider the so-called Arnold–Beltrami–Childress flow, which is known to be a time-independent, three-dimensional solution of Euler's equations (Dombre *et al.* 1986)

$$\left.\begin{aligned} u &= \sin z + \cos y, \\ v &= \sin x + \cos z, \\ w &= \sin y + \cos x. \end{aligned}\right\} \tag{3.7}$$

Unlike the two-dimensional BC flow previously considered, in this flow configuration the Lagrangian fluid elements show both regular and chaotic trajectories, depending on their initial position (Biferale *et al.* 1995). A detailed analysis of this dynamical system can be found in Dombre *et al.* (1986).

In figure 6(*a,c,e,g*) we present the results of our analysis for this 3-D case. As for the BC flow, we find that for sufficiently low Stokes numbers, i.e. $St \leqslant 0.1$, the agreement is evident between the fluid and fibre transverse velocity differences. Like the 2-D case and as expected, the agreement deteriorates for increasing St.

Downloaded from https://www.cambridge.org/core. Sistema Bibliotecario - Universita degli Studi di Genova, on 30 May 2020 at 05:05:56, subject to the Cambridge Core terms of use, available at https://www.cambridge.org/core/terms.
https://doi.org/10.1017/jfm.2020.288

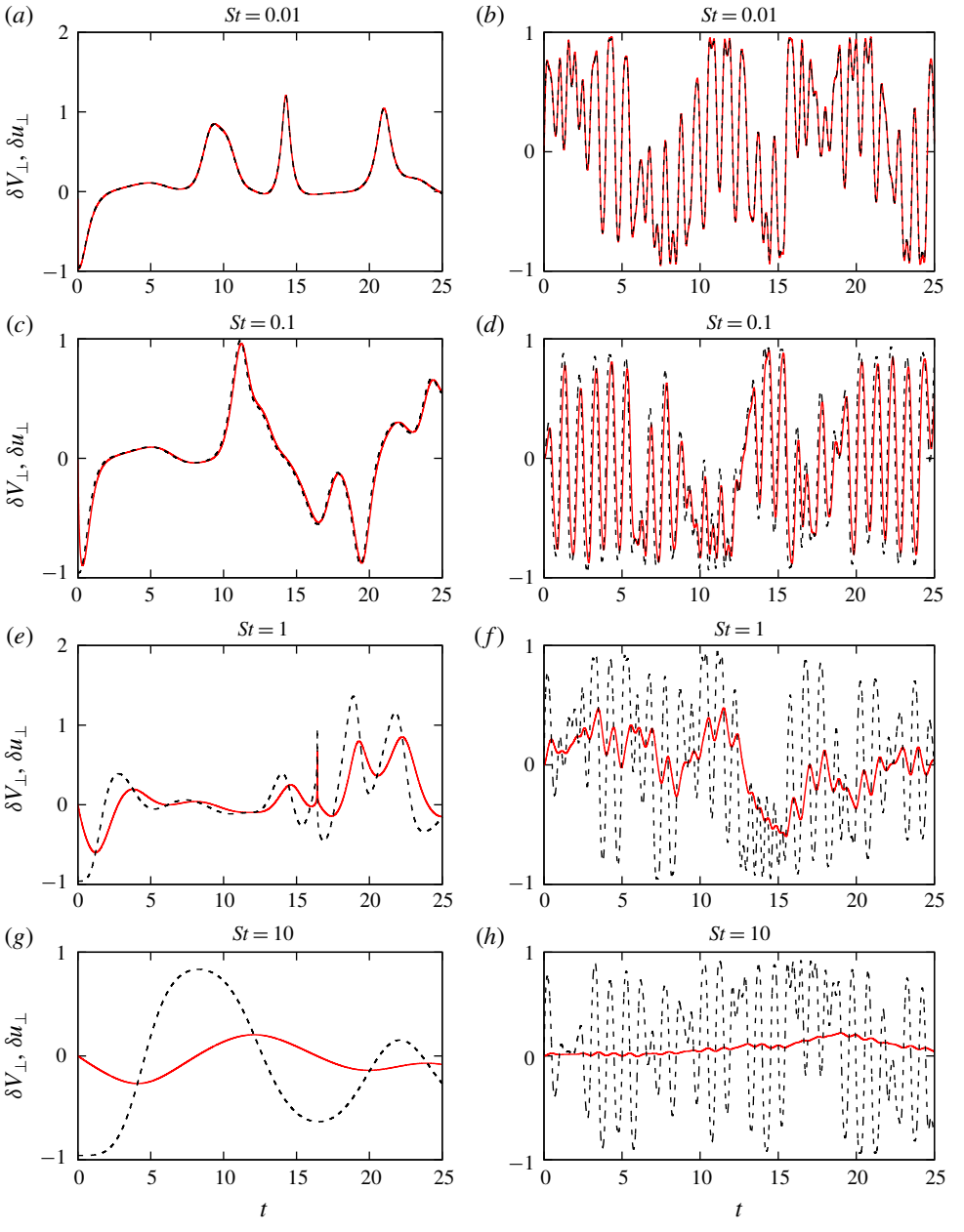

FIGURE 6. Transverse velocity differences of fibre $\delta V_\perp$ (solid line) and unperturbed flow $\delta u_\perp$ (dashed line) for different Stokes numbers, computed using the passive model. (*a,c,e,g*) ABC flow (3.7); (*b,d,f,h*), 2-D oscillating cellular flow (equation (3.8)). The normalized root mean square deviation between $\delta V_\perp$ and $\delta u_\perp$, for both ABC flow and 2-D oscillating flow, is less than 1 % for $St \leqslant 0.1$, of the order of 15 % for $St = 1$ and larger than 20 % for $St = 10$.

Next, we present the results for the unsteady, i.e. time-periodic, and two-dimensional flow

$$\left.\begin{aligned} u &= \sin[x + \epsilon_1 \sin(\omega_1 t)] \cos[y + \epsilon_2 \sin(\omega_2 t)], \\ v &= -\cos[x + \epsilon_1 \sin(\omega_1 t)] \sin[y + \epsilon_2 \sin(\omega_2 t)], \end{aligned}\right\} \tag{3.8}$$

Downloaded from https://www.cambridge.org/core. Sistema Bibliotecario - Universita degli Studi di Genova, on 30 May 2020 at 05:05:56, subject to the Cambridge Core terms of use, available at https://www.cambridge.org/core/terms.
https://doi.org/10.1017/jfm.2020.288

where $\epsilon_1 = \epsilon_2 = 0.2L$ are the amplitudes while $\omega_1 = 2\pi$ and $\omega_2 = 1$ are the frequencies of the oscillation along x and y, respectively. This choice corresponds to a situation where the Lagrangian trajectories of fluid particles are chaotic (Castiglione *et al.* 1998; Cartwright *et al.* 2010). The projected velocity differences are shown in figure 6(*b,d,f,h*), where the same conclusions drawn for steady configurations are confirmed: the agreement between the fibre-based measurement and the direct evaluation using the flow expression (3.8) increases by decreasing the rotational Stokes number.

3.3. *Evaluation of the velocity gradient tensor*

Having characterized the behaviour of single fibres, we can move further, focusing on how to access the full velocity gradient tensor $\partial_j u_i$ and not only its normal-directional projection. This will be achieved by assembling several fibres in a suitable way and exploiting the following idea: for each fibre, equation (3.6) holds, where the velocity gradient becomes the unknown variable if we use $\delta V_\perp$ (that is measured by tracking the fibre trajectory) in place of D. Considering an assembly made by N_f fibres, we thus have a system of N_f equations, from which the gradient can be obtained.

Let us therefore estimate the number of fibres that are needed in the two-dimensional case: here $\partial_j u_i$ is made by 2×2 elements; however, the number of independent quantities is reduced of one by exploiting incompressibility. Hence, the assembly has to be made by $N_f = 3$ fibres, yielding the following system to be solved:

$$\left.\begin{aligned} \delta V_\perp^{(1)} &= \partial_j u_i \hat{r}_j^{(1)} \hat{r}_i^{\perp(1)}, \\ \delta V_\perp^{(2)} &= \partial_j u_i \hat{r}_j^{(2)} \hat{r}_i^{\perp(2)}, \\ \delta V_\perp^{(3)} &= \partial_j u_i \hat{r}_j^{(3)} \hat{r}_i^{\perp(3)}. \end{aligned}\right\} \tag{3.9}$$

In this system the final number of unknowns is three (i.e. three components of $\partial_j u_i$ out of four because of the incompressibility condition). Both the left-hand side of the equations and the coefficients of the velocity derivative tensor are easily measurable at each time step along the fibre trajectories and thus known from the numerical experiments. The system can be thus easily solved at each time step while following the fibre along its trajectory.

The three fibres will be connected at their centroids (numerically, it is convenient to realize these connections using springs with sufficiently high stiffness so that the distance between centroids is negligible). However, we shall let each fibre behave as in the single case, its dynamics not being substantially altered by the link with the others. To this end, it is crucial to avoid any rotational restraint, so that fibres are able to rotate freely with respect to each other. For the assembly, we measured the rotational Stokes number following the same procedure described in § 3.1.1 for the single fibre. The resulting relaxation times of each fibre composing the assembly turned out to be the same as the rotational Stokes time of the single isolated fibre. One can thus conclude that the Stokes time of the assembly is the same as that of a single fibre.

Now we are ready to test the outlined concept in the steady BC flow already used in § 3.1. As a first step, we look at the resulting time histories of the projected velocity difference for each fibre composing the assembly (figure 7), recovering the same evidence found in the case of single fibres. This provides a clue that also in this configuration it is possible to capture the features of the fluid flow. Indeed, we proceed to combine the information from all fibres, finally obtaining the velocity gradient tensor as shown in figure 8, where the time series of each element of $\partial_j u_i$ is

Downloaded from https://www.cambridge.org/core. Sistema Bibliotecario - Universita degli Studi di Genova, on 30 May 2020 at 05:05:56, subject to the Cambridge Core terms of use, available at https://www.cambridge.org/core/terms.
https://doi.org/10.1017/jfm.2020.288

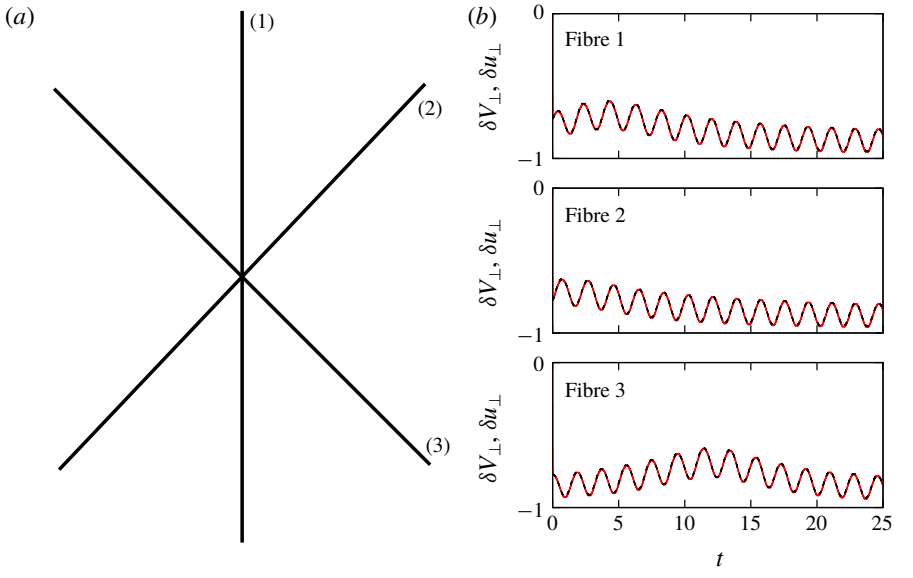

FIGURE 7. (*a*) Sketch of fibre assembly. (*b*) Transverse velocity differences of each fibre $\delta V_\perp$ (solid line) and underlying unperturbed flow $\delta u_\perp$ (dashed line) in the case of BC flow with $c = 1$ and $St \approx 0.01$, computed using the active model.

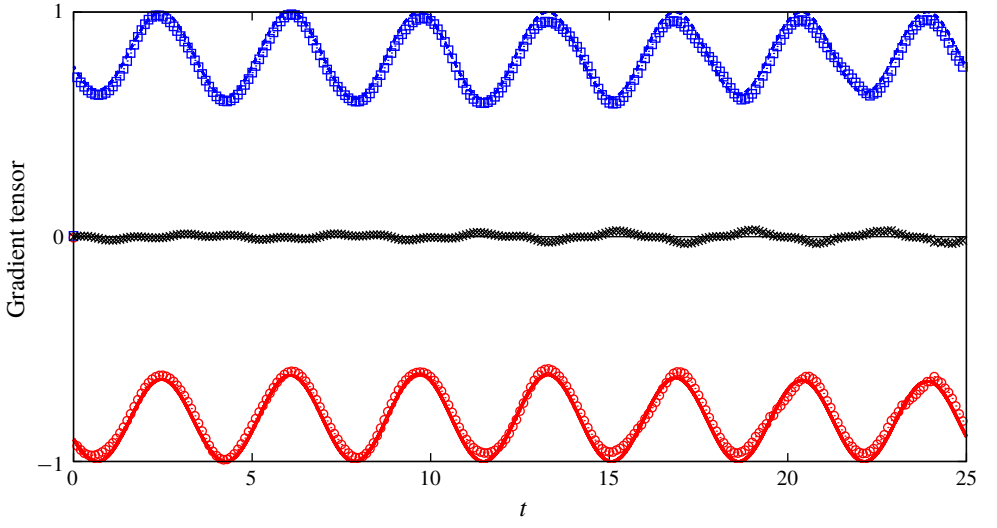

FIGURE 8. Velocity gradient tensor components in the BC flow (3.2) reconstructed by tracking the fibre assembly with $St \approx 0.01$, using the active model. Red circles, $\partial_y u$ obtained by the fibre Lagrangian tracking; red solid line, $\partial_y u$ for the unperturbed flow; blue squares, $\partial_x v$ obtained by the fibre Lagrangian tracking; blue dashed line, $\partial_x v$ for the unperturbed flow; black crosses, $\partial_x u = -\partial_y v$ obtained by the fibre Lagrangian tracking; black line, $\partial_x u = -\partial_y v = 0$ for the unperturbed flow. The normalized root mean square error between the components of the gradient tensor reconstructed by the Lagrangian tracking and those of the unperturbed flow is of the order of 1 %.

Downloaded from https://www.cambridge.org/core. Sistema Bibliotecario - Universita degli Studi di Genova, on 30 May 2020 at 05:05:56, subject to the Cambridge Core terms of use, available at https://www.cambridge.org/core/terms.
https://doi.org/10.1017/jfm.2020.288

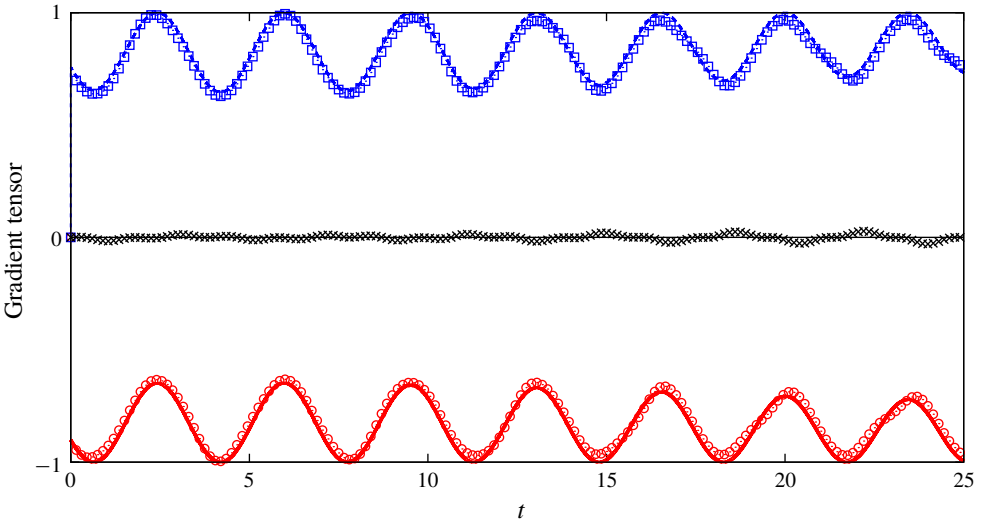

FIGURE 9. As in figure 8 but for assembly of passive fibres. The normalized root mean square error between the components of the gradient tensor reconstructed by the Lagrangian tracking and those of the unperturbed flow is of the order of 1 %.

reported, both for the fibre Lagrangian tracking and for the corresponding analytical value of the unperturbed flow. The comparison between the two quantities yields good agreement, with differences that are ascribed to numerical resolution and the finite inertia of fibres.

The reported results are for the active model but very similar evidence is obtained using the passive model. In figure 9 we show the result for the assembly of passive fibres in the static BC flow, highlighting essentially the same behaviour obtained in the active case (note that the same initial condition for the assembly of fibres was used in both cases). Finally, we complement the analysis by employing an assembly of passive fibres in the oscillating two-dimensional flow introduced in § 3.2, equation (3.8). Results are shown in figure 10 from which we can confirm the same conclusion as outlined before.

It is worth noting that the linear system (3.9) we numerically solved to obtain all components of the flow gradient can become overdetermined because of the alignment of two of more fibres. To avoid this problem we found that the simple recipe of imposing a small displacement (of Δs, the size of the Lagrangian mesh) between the centroids of the fibres of the assembly (instead of imposing them to be zero) is enough to prevent perfect alignment of the fibres, thus preventing the breakdown of the solution. The results reported in figures 8–10 have been obtained exploiting this simple, but effective, strategy. Figure 11 reports the time history of the angle of the three fibres composing the assembly, in the oscillating two-dimensional flow. As shown in figure, in the considered time frame the alignment between the fibres does not occur and the minimum value of the standard deviation between the three angles is 0.18 rad. Extending the time frame (not shown), up to 25, the minimum value of the standard deviation we measured was 0.0085 rad which was, however, large enough to accurately solve the system.

Downloaded from https://www.cambridge.org/core. Sistema Bibliotecario - Universita degli Studi di Genova, on 30 May 2020 at 05:05:56, subject to the Cambridge Core terms of use, available at https://www.cambridge.org/core/terms.
https://doi.org/10.1017/jfm.2020.288

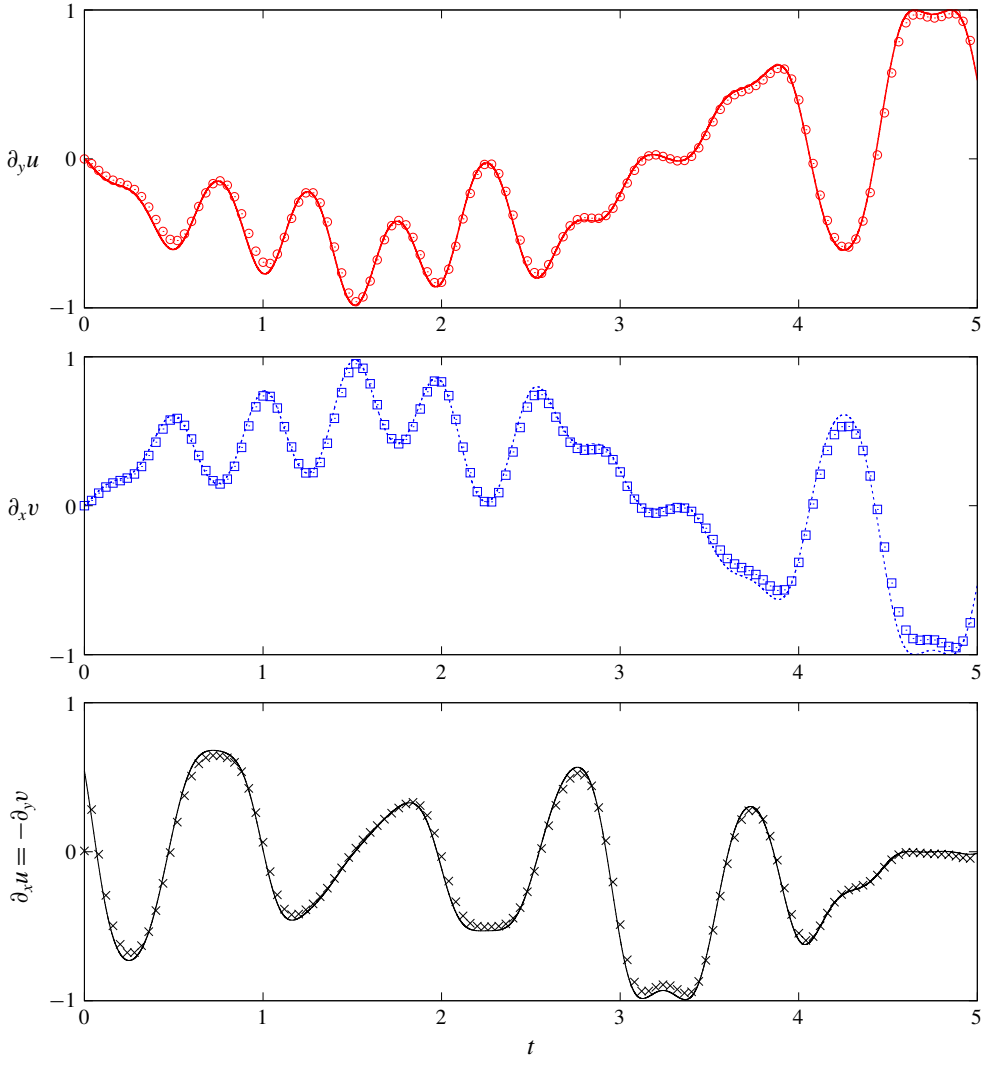

FIGURE 10. As in figure 9 but for the oscillating two-dimensional flow (3.8) (the figure is split into three panels for a better readability of the gradient tensor components). The normalized root mean square error between the components of the gradient tensor reconstructed by the Lagrangian tracking and those of the unperturbed flow is of the order of 1 %.

4. Conclusions and perspectives

This study focused on the capability of measuring the whole structure of the velocity gradient in steady, unsteady regular and chaotic cellular flows by means of Lagrangian tracking of assembly of rigid fibres. Two different kinds of fibre models have been considered: a fully coupled fibre described in terms of an immersed-boundary method and a passive fibre described by the slender body theory. We first characterized the role of fibre inertia by defining a rotational Stokes number, which is evaluated as a function of the fibre linear density. Hence, considering the velocity difference between the fibre end points and the same difference concerning

Downloaded from https://www.cambridge.org/core. Sistema Bibliotecario - Universita degli Studi di Genova, on 30 May 2020 at 05:05:56, subject to the Cambridge Core terms of use, available at https://www.cambridge.org/core/terms.
https://doi.org/10.1017/jfm.2020.288

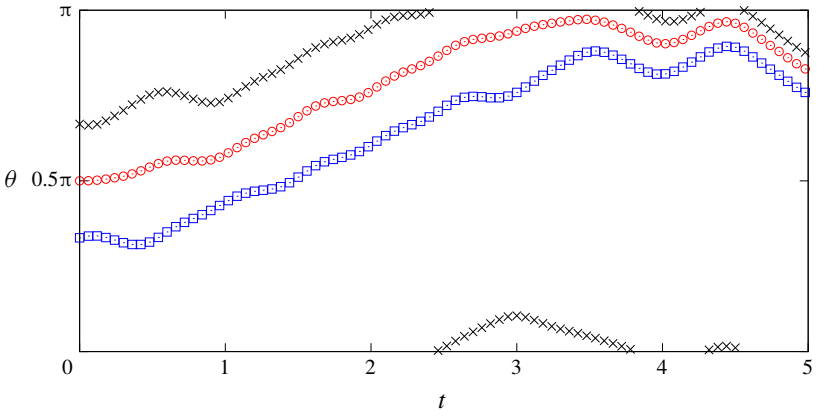

FIGURE 11. Time history of the angles (rad) of the three fibres composing the assembly in the two-dimensional oscillating flow. Red circles, fibre 1; blue squares, fibre 2; black crosses, fibre 3. Angles are measured with respect to the horizontal direction. The minimum value of the standard deviation is 0.18.

the underlying fluid velocity, both projected along the normal direction to the fibre, we showed that the fibre turns out to be a proxy of such two-point quantity. For sufficiently small fibres, this two-point quantity reduces to the transverse component of the flow velocity derivative along the fibre direction. Furthermore, the comparison between results obtained for the active model and the passive model suggests that the coupling between the flow and the fibre could be neglected, at least for small St.

This capability of using rigid fibres as a way of measuring flow properties has potential applications in experimental techniques allowing us to access small-scale, multi-point properties of fluid flows, offering an alternative to other methods that have been proposed which rely on complex elaborations using PIV/PTV (Hoyer *et al.* 2005; Krug *et al.* 2014; Lawson & Dawson 2014). Future work will thus be devoted to the practical implementation of the outlined concept in a laboratory environment. Preliminary results in this direction considering rigid fibres of millimetric size dispersed in turbulent flow appear very encouraging (Brizzolara 2019), confirming the validity of our idea in a framework well beyond the laminar/chaotic examples analysed here. The applicability of the concept can thus be extended to three-dimensional and/or turbulent flows, along with considering assemblies of fibres that would be able to measure the full structure of the velocity gradient.

Acknowledgements

The authors warmly acknowledge A. A. Banaei, M. E. Rosti and L. Brandt (KTH, Sweden) for sharing an initial version of the code for the active solver. CINECA and INFN are also acknowledged for the availability of high performance computing resources and support. A.M. thanks the financial support from the Compagnia San Paolo, project MINIERA no. I34I20000380007.

Declaration of interests

The authors report no conflict of interest.

Downloaded from https://www.cambridge.org/core. Sistema Bibliotecario - Universita degli Studi di Genova, on 30 May 2020 at 05:05:56, subject to the Cambridge Core terms of use, available at https://www.cambridge.org/core/terms. https://doi.org/10.1017/jfm.2020.288

Appendix A. Immersed boundary method

This appendix presents the numerical procedure regarding the active approach introduced in § 2.1. The Navier–Stokes equations (2.5) and (2.6) are solved for a cubic domain of side L with periodic boundary conditions in all directions, which is discretized into a Cartesian grid using N points per side. The solution is obtained by using a finite difference, fractional step method on a staggered grid with fully explicit space discretization and third-order Runge–Kutta scheme for advancement in time. Finally, the resulting Poisson equation enforcing incompressibility is solved using a fast Fourier transform.

As for the fibre-flow interaction, we employ the IB approach of Huang *et al.* (2007) and later modified by Banaei *et al.* (2020). The Lagrangian forcing is first evaluated at each fibre point, in order to enforce the no-slip condition $\dot{\boldsymbol{X}} = \boldsymbol{U}(\boldsymbol{X}(s, t), t)$, as

$$\boldsymbol{F}(s, t) = \beta\,(\dot{\boldsymbol{X}} - \boldsymbol{U}), \tag{A 1}$$

where β is a large negative constant (Huang *et al.* 2007) and

$$\boldsymbol{U}(\boldsymbol{X}(s, t), t) = \int \boldsymbol{u}(\boldsymbol{x}, t)\delta(\boldsymbol{x} - \boldsymbol{X}(s, t))\,\mathrm{d}\boldsymbol{x} \tag{A 2}$$

is the interpolated fluid velocity at the Lagrangian point. A spreading is thus performed over the surrounding Eulerian points, yielding the volumetric forcing acting on the flow

$$\boldsymbol{f}(\boldsymbol{x}, t) = \int \boldsymbol{F}(s, t)\delta(\boldsymbol{x} - \boldsymbol{X}(s, t))\,\mathrm{d}s. \tag{A 3}$$

Both the interpolation and spreading feature the Dirac operator, which in discretization terms is transposed into the use of regularized δ; in our case, we employ the function proposed by Roma, Peskin & Berger (1999).

The described procedure has been implemented and extensively validated in both laminar and turbulent flow conditions. For related information, the reader is referred to Rosti & Brandt (2017), Rosti *et al.* (2018*b*), Shahmardi *et al.* (2019), Rosti *et al.* (2020) and Banaei *et al.* (2020).

REFERENCES

ADRIAN, R. J. 1991 Particle-imaging techniques for experimental fluid mechanics. *Annu. Rev. Fluid Mech.* **23** (1), 261–304.

ALLENDE, S., HENRY, C. & BEC, J. 2018 Stretching and buckling of small elastic fibers in turbulence. *Phys. Rev. Lett.* **121**, 154501.

BAGHERI, S., MAZZINO, A. & BOTTARO, A. 2012 Spontaneous symmetry breaking of a hinged flapping filament generates lift. *Phys. Rev. Lett.* **109**, 154502.

BAKHUIS, D., MATHAI, V., VERSCHOOF, R. A., EZETA, R., LOHSE, D., HUISMAN, S. G. & SUN, C. 2019 Statistics of rigid fibers in strongly sheared turbulence. *Phys. Rev.* F **4**, 072301.

BANAEI, A. A., ROSTI, M. E. & BRANDT, L. 2020 Numerical study of filament suspensions at finite inertia. *J. Fluid Mech.* **882**, A5.

BEC, J., BIFERALE, L., BOFFETTA, G., CELANI, A., CENCINI, M., LANOTTE, A., MUSACCHIO, S. & TOSCHI, F. 2006 Acceleration statistics of heavy particles in turbulence. *J. Fluid Mech.* **550**, 349–358.

BEC, J., BIFERALE, L., CENCINI, M., LANOTTE, A., MUSACCHIO, S. & TOSCHI, F. 2007 Heavy particle concentration in turbulence at dissipative and inertial scales. *Phys. Rev. Lett.* **98**, 084502.

Downloaded from https://www.cambridge.org/core. Sistema Bibliotecario - Universita degli Studi di Genova, on 30 May 2020 at 05:05:56, subject to the Cambridge Core terms of use, available at https://www.cambridge.org/core/terms. https://doi.org/10.1017/jfm.2020.288

BIFERALE, L., CRISANTI, A., VERGASSOLA, M. & VULPIANI, A. 1995 Eddy diffusivities in scalar transport. *Phys. Fluids* **7** (11), 2725–2734.

BOUNOUA, S., BOUCHET, G. & VERHILLE, G. 2018 Tumbling of inertial fibers in turbulence. *Phys. Rev. Lett.* **121**, 124502.

BRIZZOLARA, S. 2019 Fiber tracking velocimetry. Master thesis, University of Genova.

BUTLER, J. E. & SNOOK, B. 2018 Microstructural dynamics and rheology of suspensions of rigid fibers. *Annu. Rev. Fluid Mech.* **50** (1), 299–318.

CARTWRIGHT, J. H. E., FEUDEL, U., KÁROLYI, G., DE MOURA, A., PIRO, O. & TÉL, T. 2010 *Dynamics of Finite-Size Particles in Chaotic Fluid Flows*. Springer.

CASTIGLIONE, P., CRISANTI, A., MAZZINO, A., VERGASSOLA, M. & VULPIANI, A. 1998 Resonant enhanced diffusion in time-dependent flow. *J. Phys.* A*: Math. Gen.* **31** (35), 7197–7210.

CHOUIPPE, A. & UHLMANN, M. 2015 Forcing homogeneous turbulence in direct numerical simulation of particulate flow with interface resolution and gravity. *Phys. Fluids* **27** (12), 123301.

COX, R. G. 1970 The motion of long slender bodies in a viscous fluid Part 1. General theory. *J. Fluid Mech.* **44** (4), 791–810.

DO-QUANG, M., AMBERG, G., BRETHOUWER, G. & JOHANSSON, A. V. 2014 Simulation of finite-size fibers in turbulent channel flows. *Phys. Rev.* E **89**, 013006.

DOMBRE, T., FRISCH, U., GREENE, J. M., HÉNON, M., MEHR, A. & SOWARD, A. M. 1986 Chaotic streamlines in the ABC flows. *J. Fluid Mech.* **167**, 353–391.

EATON, J. K. & FESSLER, J. R. 1994 Preferential concentration of particles by turbulence. *Intl J. Multiphase Flow* **20**, 169–209.

GUSTAVSSON, K., SHEIKH, M. Z., LOPEZ, D., NASO, A., PUMIR, A. & MEHLIG, B. 2019 Effect of fluid inertia on the orientation of a small prolate spheroid settling in turbulence. *New J. Phys.* **21** (8), 083008.

HEJAZI, B., KRELLENSTEIN, M. & VOTH, G. A. 2019 Using deformable particles for single-particle measurements of velocity gradient tensors. *Exp. Fluids* **60** (10), 153.

HOYER, K., HOLZNER, M., LÜTHI, B., GUALA, M., LIBERZON, A. & KINZELBACH, W. 2005 3D scanning particle tracking velocimetry. *Exp. Fluids* **39** (5), 923.

HUANG, W.-X., SHIN, S. J. & SUNG, H. J. 2007 Simulation of flexible filaments in a uniform flow by the immersed boundary method. *J. Comput. Phys.* **226** (2), 2206–2228.

JEFFERY, G. B. 1922 The motion of ellipsoidal particles immersed in a viscous fluid. *Proc. R. Soc. Lond.* A **102** (715), 161–179.

KRUG, D., HOLZNER, M., LÜTHI, B., WOLF, M., TSINOBER, A. & KINZELBACH, W. 2014 A combined scanning PTV/LIF technique to simultaneously measure the full velocity gradient tensor and the 3D density field. *Meas. Sci. Technol.* **25** (6), 065301.

KUPERMAN, S., SABBAN, L. & VAN HOUT, R. 2019 Inertial effects on the dynamics of rigid heavy fibers in isotropic turbulence. *Phys. Rev.* F **4**, 064301.

LĀCIS, U., BROSSE, N., INGREMEAU, F., MAZZINO, A., LUNDELL, F., KELLAY, H. & BAGHERI, S. 2014 Passive appendages generate drift through symmetry breaking. *Nat. Commun.* **5**, 5310.

LĀCIS, U., OLIVIERI, S., MAZZINO, A. & BAGHERI, S. 2017 Passive control of a falling sphere by elliptic-shaped appendages. *Phys. Rev.* F **2**, 033901.

LAWSON, J. M. & DAWSON, J. R. 2014 A scanning PIV method for fine-scale turbulence measurements. *Exp. Fluids* **55** (12), 1857.

MARCHIOLI, C., FANTONI, M. & SOLDATI, A. 2010 Orientation, distribution, and deposition of elongated, inertial fibers in turbulent channel flow. *Phys. Fluids* **22** (3), 033301.

MARCHIOLI, C., ZHAO, L. & ANDERSSON, H. I. 2016 On the relative rotational motion between rigid fibers and fluid in turbulent channel flow. *Phys. Fluids* **28** (1), 013301.

NI, R., KRAMEL, S., OUELLETTE, N. T. & VOTH, G. A. 2015 Measurements of the coupling between the tumbling of rods and the velocity gradient tensor in turbulence. *J. Fluid Mech.* **766**, 202–225.

PARSA, S., CALZAVARINI, E., TOSCHI, F. & VOTH, G. A. 2012 Rotation rate of rods in turbulent fluid flow. *Phys. Rev. Lett.* **109**, 134501.

Downloaded from https://www.cambridge.org/core. Sistema Bibliotecario - Universita degli Studi di Genova, on 30 May 2020 at 05:05:56, subject to the Cambridge Core terms of use, available at https://www.cambridge.org/core/terms. https://doi.org/10.1017/jfm.2020.288

QUENNOUZ, N., SHELLEY, M., DU ROURE, O. & LINDNER, A. 2015 Transport and buckling dynamics of an elastic fibre in a viscous cellular flow. *J. Fluid Mech.* **769**, 387–402.

ROMA, A. M., PESKIN, C. S. & BERGER, M. J. 1999 An adaptive version of the immersed boundary method. *J. Comput. Phys.* **153** (2), 509–534.

ROSTI, M. E., BANAEI, A. A., BRANDT, L. & MAZZINO, A. 2018*a* Flexible fiber reveals the two-point statistical properties of turbulence. *Phys. Rev. Lett.* **121**, 044501.

ROSTI, M. E. & BRANDT, L. 2017 Numerical simulation of turbulent channel flow over a viscous hyper-elastic wall. *J. Fluid Mech.* **830**, 708–735.

ROSTI, M. E., IZBASSAROV, D., TAMMISOLA, O., HORMOZI, S. & BRANDT, L. 2018*b* Turbulent channel flow of an elastoviscoplastic fluid. *J. Fluid Mech.* **853**, 488–514.

ROSTI, M. E., OLIVIERI, S., BANAEI, A. A., BRANDT, L. & MAZZINO, A. 2020 Flowing fibers as a proxy of turbulence statistics. *Meccanica* **55**, 357–370.

DU ROURE, O., LINDNER, A., NAZOCKDAST, E. N. & SHELLEY, M. J. 2019 Dynamics of flexible fibers in viscous flows and fluids. *Annu. Rev. Fluid Mech.* **51** (1), 539–572.

SABBAN, L., COHEN, A. & VAN HOUT, R. 2017 Temporally resolved measurements of heavy, rigid fibre translation and rotation in nearly homogeneous isotropic turbulence. *J. Fluid Mech.* **814**, 42–68.

SCHANZ, D., GESEMANN, S. & SCHRÖDER, A. 2016 Shake-the-box: Lagrangian particle tracking at high particle image densities. *Exp. Fluids* **57** (5), 70.

SHAHMARDI, A., ZADE, S., ARDEKANI, M. N., POOLE, R. J., LUNDELL, F., ROSTI, M. E. & BRANDT, L. 2019 Turbulent duct flow with polymers. *J. Fluid Mech.* **859**, 1057–1083.

SHELLEY, M. J. & ZHANG, J. 2011 Flapping and bending bodies interacting with fluid flows. *Annu. Rev. Fluid Mech.* **43**, 449–465.

TORNBERG, A.-K. & SHELLEY, M. J. 2004 Simulating the dynamics and interactions of flexible fibers in Stokes flows. *J. Comput. Phys.* **196** (1), 8–40.

VOTH, G. A. & SOLDATI, A. 2017 Anisotropic particles in turbulence. *Annu. Rev. Fluid Mech.* **49** (1), 249–276.

WANDERSMAN, E., QUENNOUZ, N., FERMIGIER, M., LINDNER, A. & DU ROURE, O. 2010 Buckled in translation. *Soft Matt.* **6**, 5715–5719.

YOUNG, Y. N. & SHELLEY, M. J. 2007 Stretch-coil transition and transport of fibers in cellular flows. *Phys. Rev. Lett.* **99**, 058303.

Downloaded from https://www.cambridge.org/core. Sistema Bibliotecario - Universita degli Studi di Genova, on 30 May 2020 at 05:05:56, subject to the Cambridge Core terms of use, available at https://www.cambridge.org/core/terms. https://doi.org/10.1017/jfm.2020.288